Journal Name

ARTICLE TYPE

Cite this: DOI: 00.0000/xxxxxxxxxx

# Computational Studies of Shape Control of Charged Deformable Nanocontainers†

Nicholas E. Brunk,[a] and Vikram Jadhao,[b]

Received Date
Accepted Date

DOI: 00.0000/xxxxxxxxxx

Biological matter is often compartmentalized by soft membranes that dynamically change their shape in response to chemical and mechanical cues. Deformable soft-matter-based nanoscale membranes or nanocontainers that mimic this behavior can be used as drug-delivery carriers that can adapt to evolving physiological conditions, or as dynamic building blocks for the design of novel hierarchical materials via assembly engineering. Here, we connect the intrinsic features of charged deformable nanocontainers such as their size, charge, surface tension, and elasticity with their equilibrium shapes for a wide range of solution conditions using molecular dynamics simulations. These links identify the fundamental mechanisms that establish the chemical and materials design control strategies for modulating the equilibrium shape of these nanocontainers. We show that flexible nanocontainers of radii ranging from 10 - 20 nm exhibit sphere-to-rod-to-disc shape transitions yielding rods and discs over a wide range of aspect ratio $\lambda$ ($0.3 < \lambda < 5$). The shape transitions can be controlled by tuning salt and/or surfactant concentration as well as material elastic parameters. The shape changes are driven by reduction in the global electrostatic energy and are associated with dramatic changes in local surface elastic energy distributions. To illustrate the shape transition mechanisms, exact analytical calculations for idealized spheroidal nanocontainers in salt-free conditions are performed. Explicit counterion simulations near nanocontainers and associated Manning model calculations provide an assessment of the stability of observed shape deformations in the event of ion condensation.

## 1 Introduction

Deformable soft-matter-based nanocontainers offer unprecedented opportunities for applications in nanomedicine and developing bio-inspired reconfigurable materials. Soft-matter-based nanosystems such as polymeric nanomembranes, micellar vesicles, and protein nanocages can serve as drug-carrying containers that dynamically change shape, adapting to evolving physiological conditions[1,2]. Experiments have shown that the shape of these nanoparticles modulates their biodistribution and cellular uptake, ultimately affecting the therapeutic response[1,3–10]. For example, recent research has shown that rod-shaped micelles have longer circulation times than their spherical counterparts[11], and disc-shaped nanoparticles demonstrate higher in vivo targeting specificity for cells expressing adhesive receptors than similarly-sized spherical nanoparticles[12]. Generally, endocytosis studies have shown uptake sensitivity to rod and disc-like morphologies[13–15].

Shape-changing nanoparticles and microparticles also offer the prospects of being utilized as dynamic building blocks for the design of new materials via assembly engineering[16–18]. These deformable nanoparticles offer access to unique assembly pathways inaccessible to static building blocks, and are expected to yield novel hierarchical structures. Such structures can be self-assembled using a variety of strategies and control mechanisms extensively developed to assemble rigid building blocks for many applications including photonics and catalysis[19–24].

Experimental advances in nanotechnology and materials chemistry have revolutionized our ability to fabricate nanoparticles with exquisite control of surface properties[25–27]. More recently, nanoparticles, including hollow nanocontainers, with the ability to change shape in response to environmental cues have been synthesized[28–31]. To connect experimental advances in surface property regulation to the design of deformable nanocontainers, we need to establish the link between the nanocontainer surface physicochemical properties and their energetically-favored shapes. Associated fundamental mechanisms are especially lacking for the design of nanocontainers that change shape by altering the nanocontainer electrostatic properties or surface tension.

Changing the shape of nanoscale containers entails bending

[a] Intelligent Systems Engineering, Indiana University, Bloomington, Indiana 47408, USA. E-mail: nbrunk@iu.edu
[b] Intelligent Systems Engineering, Indiana University, Bloomington, Indiana 47408, USA. Tel: 812-856-4018; E-mail: vjadhao@iu.edu

and stretching it, and the associated energy costs form the elastic components of the free energy of the container. Theoretically, shape manipulation in uncharged, deformable membranes has been explored by topological defects[32–34], compression, and the use of surface inhomogeneities[35,36]. A key goal has been to find the low-energy conformations of these soft elastic membranes under different geometric and material constraints. When the membrane is charged, it is possible to compensate for the increase in elastic energy associated with the shape deformation by significantly lowering the electrostatic free energy[37–39]. However, due to the complexity of the ensuing problem, the interplay between electrostatic interactions and the structure of charged deformable membranes is far less understood.

Early work on charged elastic membranes (shells) mainly focused on mapping a charged, deformable membrane to an uncharged, deformable membrane with charge-renormalized elastic parameters[40–42]. Recent studies have modeled Coulomb interactions explicitly to accurately describe the nonlinear coupling between elastic and electrostatic forces in charged nanoscale containers where the surface charge density can assume high values ($\gtrsim 0.1e/\text{ nm}^2$)[38,43,44]. Using such models, it has been shown that an ionic shell, where positive and negative charges populate the surface, lowers its energy by taking a faceted (icosahedral) shape with the same surface area[43].

Using a similar coarse-grained model that included explicit Coulomb and elastic forces, we previously demonstrated that shape deformation occurs under a volume constraint with symmetry breaking along one or more axes to form disc or concave bowl conformations, respectively[39]. By virtue of the electrostatics-driven deformation, environmental (solution-based) control strategies (e.g., tuning salt concentration) as well as materials design approaches (e.g., tuning surface charge) were demonstrated as a feasible means of controlling container shape and changing preferences for bowl-like or disc-like morphologies. Effects of ion condensation were analyzed using a two-state Manning mean-field model, which supported the feasibility of the observed shape transitions[39,44].

Building on our previous studies, here we design a minimal coarse-grained model of a flexible nanomembrane representative of monolayer vesicles and protein nanocages in electrolyte solution to establish the links between surface properties of uniformly-charged, volume-conserving deformable nanocontainers and their equilibrium shapes by using molecular dynamics (MD) simulations[39,44]. We systematically explore the design space generated by the nanocontainer size, surface charge, bending rigidity $\kappa_b$, stretching constant $\kappa_s$, and the bulk solution salt concentration and interfacial surface tension to show that flexible nanocontainers of radii ranging from 10 - 20 nm exhibit sphere-to-rod-to-disc shape transitions. Rods and discs of varying aspect ratio $\lambda$ spanning a wide range of $0.3 < \lambda < 5$ are observed. The shape changes can be controlled by tuning surface tension ($\approx 0-10$ dynes/cm) and/or salt concentration ($0.5-50$ mM) as well as material elastic parameters ($\kappa_b, \kappa_s \in (1,100)k_BT$). The shape changes are driven by reduction in the global electrostatic energy and are associated with dramatic changes in local surface elastic energy distributions. To illustrate the shape transition mechanisms, exact analytical calculations for idealized spheroidal nanocontainers in salt-free conditions are performed. Explicit counterion simulations near nanocontainers and associated Manning model calculations provide an assessment of the stability of observed shape deformations in the event of ion condensation.

Results of the investigations expand upon both the solution-based control strategies and materials design strategies for development of shape-adaptable nanocontainers, and show that shapes of similar aspect ratios can be obtained for different nanocontainer sizes. Surface tension of the nanocontainer serves as both a solution-based control and materials design control strategy, in that it can be tuned by changing the bulk surfactant concentration or by modifying the hydrophobic surface chemistry of the nanocontainer. In addition to exploring the dependence of shapes on chemical controls, the material design subspace spanned by stretching and bending elastic moduli is also explored, showing that controlling the elastic properties of the nanocontainer can modulate the preference for rod/disc morphologies. These fundamental studies provide initial insights into the design of deformable nanocontainers for nanomedicine applications and the synthesis of dynamic building blocks for application in electrostatically-controlled assembly engineering[19,20,45].

## 2 Model and Simulation Methods

### 2.1 Coarse-grained triangulated-network model

Fully atomistic particle-based models that explicitly account for each atom are important in studying nanocontainer surface interactions with small molecules and associated short-time dynamical processes. However, for simulation of shape deformations of large nanocontainers (of radius $\gtrsim 10$ nm) considered here, this description is unfeasible. Coarse-grained particle-based models that employ effective potentials informed by atomistic simulations and experimental data offer a feasible alternative.

Suppressing atomistic details, the nanocontainer surface is represented as a thin elastic membrane consisting of $N_v$ hard, spherical beads (vertices) connected by $N_e$ flexible springs (edges), constituting faces of the discretized membrane mesh following the standard physical representation in this class of models[46–51]. For a spherical nanoparticle mesh of a given size, the discretized mesh point density is held constant, yielding approximately $N_v \approx 1000$ points on a mesh of radius $R = 10$ nm. Each vertex is associated with a charge $q = Q/N_v$ where $Q$ is the total effective surface charge. Electrostatic effects between vertices are modeled using the screened Coulomb (Yukawa) interactions.

The energy characterizing the discretized nanocontainer membrane is given by Equation 1 and includes the total bending energy (first term), stretching energy (second term), electrostatic energy (third term), and the surface energy associated with a fi-

nite membrane tension (fourth term):

$$\mathscr{H} = \frac{\kappa_b}{2}\sum_{l\in E}|\vec{n}_{l_1}-\vec{n}_{l_2}|^2 + \frac{\kappa_s}{2R^2}\sum_{l\in E}(|\vec{r}_{l_1}-\vec{r}_{l_2}|-a_l)^2 + \frac{l_B q^2}{2}\sum_{i=1}^{i=N_v}\sum_{j\neq i}^{j=N_v}\frac{e^{\frac{-|\vec{r}_i-\vec{r}_j|}{\lambda_D}}}{|\vec{r}_i-\vec{r}_j|} + \sigma_A\sum_{k\in F}A_k. \quad (1)$$

In Equation 1, $\kappa_b$ is the bending rigidity, $\kappa_s$ is the stretching constant, $R$ is the radius associated with the spherical conformation for uncharged and rigid membrane, $a_l$ is equilibrium length of edge $l$, $l_B$ is Bjerrum length, $q$ is vertex charge, $\lambda_D$ is Debye screening length, and $\sigma_A$ is surface tension. $\vec{n}$ denotes the normal vector associated with a face, $\vec{r}$ denotes the position vector of the vertex, and $A_k$ denotes the area of face $k$. Following other theoretical studies[52–54], the inclusion of the surface tension energy term in the total Hamiltonian inhibits large increase in area upon shape deformation. All the four energy components are expressed in units of $k_BT$, where $k_B$ is Boltzmann's constant and $T = 298$ K is room temperature.

Bending energy depends on the normals, $\vec{n}_{l_1}$ and $\vec{n}_{l_2}$, to the faces opposite each edge $l$ and is measured relative to the planar conformation, which is assigned zero (lowest) bending energy. In the current model, there is thus no inherent curvature to the membrane components. Stretching energy between neighboring pairs of vertices is measured relative to the equilibrium initial spherical conformation, and is characterized by the Young's modulus $Y = \kappa_s/R^2$; as the sphere is of the lowest area for a given volume, it is of zero (lowest) stretching energy. Electrostatic energies are computed between all pairs of vertices ($\vec{r}_i, \vec{r}_j$ for $i \neq j$) as screened Yukawa potentials, where the screening length $\lambda_D = 1/\sqrt{8\pi l_B I}$ depends upon the solution ionic strength $I$ (in Molar) that is related to the salt concentration $c_s$ via the equation $I = 1/2c_s(z_+^2 + z_-^2)$. Here it is assumed that we have only one type of salt with ions of valencies $z_+$ and $z_-$; the equation simplifies to $I = c_s$ for monovalent salt considered in this work. All models employ water as the implicit solvent, making $l_B \approx 0.7$ nm. Finally, the surface tension energy contribution from each face is considered to be proportional to the area $A_k$ associated with the face $k$, with the proportionality constant taken as the surface tension $\sigma_A$.

We constrain the system using a SHAKE-RATTLE algorithm to conserve the volume during shape deformations[55]. The volume constraint can be representative of an invariant amount of cargo in the nanocontainer and/or (closed) membranes that do not exchange significant matter with the environment. The volume is constrained to that of the initial spherical conformation. The undeformed spherical conformation has the smallest area and thus highest electrostatic energy, allowing electrostatic energy minimization to drive deformation under the volume constraint.

### 2.2 Shape design space

Parameters $R, Q, c_s, \sigma_A, \kappa_b, \kappa_s$ describing the above model Hamiltonian span the shape design space and serve to represent a minimal model of a nanocontainer investigated for low-energy equilibrium shapes. A summary of the parameter ranges investigated in this work is provided in Table 1.

| Parameter | Minimum | Maximum |
|---|---|---|
| Radius ($R$) | 10 nm | 20 nm |
| Effective Charge ($Q$) | $150e$ | $1050e$ |
| Salt concentration ($c_s$) | 0.5 mM | 50 mM |
| Surface Tension ($\sigma_A$) | 0 dyn/cm | 10 dyn/cm |
| Bending Modulus ($\kappa_b$) | 1 $k_BT$ | 40 $k_BT$ |
| Stretching Modulus ($\kappa_s$) | 20 $k_BT$ | 100 $k_BT$ |

**Table 1** Shape control parameters investigated in this work along with the range of values explored. Parameters include the nanocontainer radius and effective charge ($R, Q$), the solution salt concentration ($c_s$), the surface tension of the nanocontainer-solution interface ($\sigma_A$), and the bending and stretching moduli of the nanocontainer ($\kappa_b, \kappa_s$).

Nanocontainers of size in the range of $10 \leq R \leq 20$ nm are investigated. This size range is typical of micelles and spherical viruses (e.g., Hepatitis B Virus). Larger nanocontainers require greater computational resources because of larger mesh size needed to represent the continuum membrane model. Transitions occur using effective surface charges typical (or less than those) of micelles, viruses, and polymeric nanoparticles, $150e \leq Q \leq 1050e$[20,45,56,57]. Surface tension values are chosen in the range of $0 < \sigma < 10$ dynes/cm, and represent typical weak hydrophobic interactions[58] between the coarse-grained surface patches associated with the nanocontainer membrane. The broad range of size, charge, and tension parameters provide a sufficiently wide spectrum of shapes and transition control strategies for exploring the underlying mechanisms of shape deformation in charged, deformable nanocontainers. The material design parameters, bending and stretching elastic moduli, are swept over a similar wide range of values. These elastic features can be tuned by varying ligands functionalized on the nanocontainer surface (such as mechanically reinforcing proteins) and solution conditions such as reducing agents inhibiting the formation of covalent disulfide bonds between components of the nanocontainer surface[59–61]. We will invoke wherever necessary a single parameter: the Foppl-von-Karman (FvK) number defined as the ratio of the stretching to bending moduli, $\gamma = YR^2/\kappa_b = \kappa_s/\kappa_b$, to ease the discussion of the elastic energy contributions associated with the shape deformations. Over 6000 simulations spanning the parameter regimes highlighted in Table 1 were launched to obtain the data necessary to reveal shape control mechanisms.

### 2.3 Molecular dynamics based simulated annealing

The energy $\mathscr{H}$ characterizing the nanocontainer surface is a function of the set of vertex position vectors $\vec{r}_i$, which parametrize the shape of the shell. The equilibrium shape corresponds to the minimum of $\mathscr{H}$ subject to geometric constraints. The nonlinear coupling between the nanocontainer shape and its electrostatic, elastic, and surface tension energies needs to be evaluated self-consistently in order to accurately predict equilibrium shapes as a function of material and environmental control parameters. This constrained energy minimization is carried out using a molecular dynamics (MD)-based simulated annealing procedure described in our earlier work[39]. The method is accelerated using an OpenMP/MPI hybrid parallelization technique reducing the computing time for a typical simulation of a nanocontainer discretized with $N_v \approx 1000$ vertices from 40 to 4 hours by using a

32-fold greater number of cores. This acceleration enables thousands of simulations and an extensive exploration of the shape design space.

MD-based simulated annealing begins at a fictitious temperature high enough to allow the nanocontainer surface to deform and explore the energy landscape, after which kinetic energy is gradually removed from the system. This allows gradual convergence towards the fluctuating shapes of low energy (most probable shapes), and eventually the equilibrium shape. In an experimental setting at room temperature (without annealing), thermal fluctuations are expected to occur around the simulation-predicted low-energy (equilibrium) shape. In addition to predicting the equilibrium shapes of deformable nanocontainers and yielding geometric information such as nanocontainer visualizations and area $A$ that help identify shape change quantitatively, the method yields thermodynamic information such as local energy distributions (e.g., elastic) on the nanocontainer surface that correlate with shape transitions.

In quantifying shape change, coordinates of the triangulated mesh are used to extract an approximate aspect ratio of the deformed nanocontainer. An ideal prolate spheroidal (rod-like) conformation is shown in Figure 1 to illustrate the definition of the aspect ratio that is described in terms of its semi-principal axes $a,b,c$. For rods and discs produced via the energy minimization procedure in our simulations (which are not ideal prolate or oblate spheroidal shells), the aspect ratio is computed via the following process using Mathematica 12.0[62]. The mesh coordinates are imported and the geometric center (average of all coordinates) is set to zero. The longest axis associated with the shape characterized by the mesh (identified by the two vertices with the greatest separation $r_{ij}$) is aligned with the x-axis. Next, a subset of the mesh points approximately in the $x=0$ plane are selected. The vertex within this subset that is farthest from the origin identifies the second longest shape axis, which is then aligned with the y-axis. This process results in making the shortest axis of the nanocontainer align approximately with the z-axis for the shapes investigated. After these alignments, the semi-principal axes $a,b,c$ (Figure 1) are extracted as half of the maximal distance between vertices along the associated shape axes $x,y,z$ (note $a \geq b \geq c$). If $a > b \approx c$, the shape is classified as a rod and the aspect ratio is computed as $\lambda = a/c$, and when $a \approx b > c$, the shape is classified as a disc and the aspect ratio is computed as $\lambda = c/a$. In practice, the classification follows the rule: if $a-b > b-c$, the shape is a rod of aspect ratio $\lambda = a/c > 1$, otherwise the shape is classified as a disc or sphere of aspect ratio $\lambda = c/a \leq 1$.

### 2.4 MD simulations of ions near nanocontainer surface

MD-based simulated annealing to optimize the nanocontainer energy is performed using electrostatic interactions represented as Yukawa potentials (the third term in Equation 1). These interaction potentials treat the effects of ions surrounding the nanocontainer implicitly. The condensation of counterions on the nanocontainer surface may affect the electrostatics-driven shape changes in deformable nanocontainers[63]. To verify persistence of the predicted shapes and assess their stability, separate

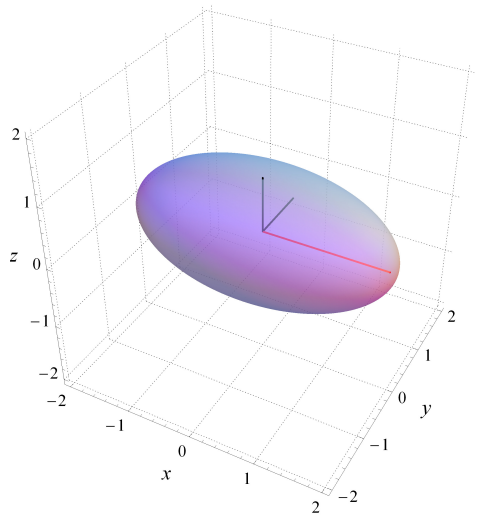


**Fig. 1** An ideal rod conformation (prolate spheroidal shell) whose surface is defined by the equation $\frac{x^2}{a^2}+\frac{y^2}{b^2}+\frac{z^2}{c^2}=1$, with semi-principal axes $a,b,c$ aligned with the $x,y,z$ axes respectively. Ideal rods and discs (oblate spheroidal shells) have two semi-principal axes equal. For example, $b=c$ highlighted by the black lines, and the longer semi-principal axis $a$ highlighted by the red. The aspect ratio of the rod is defined as $\lambda = a/c > 1$; for the rod shown, $\lambda = 2$. Values of $\lambda < 1$ correspond to discs ($\lambda = 1$ for spheres). Extraction of approximate aspect ratios for rods and discs observed in the simulations is discussed in the text.

post-optimization MD simulations are conducted wherein explicit counterions are placed in a periodic cubic box enclosing an immobile nanocontainer with a shape produced via the energy optimization process.

The nanocontainer surface is more finely meshed with 4692 to 5592 mesh points, depending on the surface area, with each point representing a counterion-sized spherical bead. Steric interactions between ions, modeled as spherical particles of $\sigma_c = 0.6$ nm diameter, and the nanocontainer surface beads were modeled using the standard purely-repulsive Lennard-Jones potential, $U_{LJ}(r) = 4((\sigma_c/r)^{12} - (\sigma_c/r)^6)$. A cutoff of $2^{1/6}\sigma_c$ is chosen to speed up calculations. Electrostatic ion-ion and ion-bead interactions are modeled using the Coulomb potential. Long-range effects are treated using the PPPM solver to compute forces between periodic images of particles in k-space[64]. Coulomb interactions between beads (mesh points) of the nanocontainer do not affect the ion dynamics, and are excluded from evaluation to improve efficiency. Simulations are performed using LAMMPS[65] in an NVT ensemble at room temperature with volume set by the packing fraction and nanocontainer size. Multiple values of packing fraction are considered to probe the effect of changing nanocontainer concentration on counterion condensation and accurately evaluate the associated changes in shape stability.

On reaching equilibrium, Diehl's method for assessing the fraction of ions condensed on the nanocontainer surface ($\alpha_c$) is employed[66]. The number of condensed ions is computed by comparing the electrostatic energy of ions binding to the nanocontainer surface ($U_{e_i}$) and the kinetic energy with which they might escape ($K_{E_i}$): if $U_{e_i} \geq \chi K_{E_i}$, the $i^{\text{th}}$ ion is considered condensed, where typically $\chi = 4/3$[66]. The ensemble average of the number of con-

densed ions ($N_c$) is computed by employing sufficiently uncorrelated samples post-equilibration. Using $N_c$, the fraction of condensed ions is evaluated as $\alpha_c = N_c/N_{tot}$. $\alpha_c$ is used to extract the effective charge on the nanocontainer surface as well as to verify predictions of the Manning two-state model[67]. Based on the simulation-tested results, for low packing fractions, the Manning model is used to predict the free energy $\mathscr{F}$ of the nanocontainer in the presence of condensed ions and assess the feasibility and stability of shapes predicted by the simulated annealing procedure. All post-processing calculations are done using parallelized code in Mathematica 12.0[62].

# 3 Results and Discussion

## 3.1 Shape Transitions

Figure 2 shows the shape transitions in the nanocontainer with effective charge of $Q = 600e$ and elastic moduli $\kappa_b = \kappa_s = 40k_BT$ when the salt concentration $c_s$ is tuned from left-to-right as $c_s = (1,5,10,15)$ mM. Transitions are shown for two values of surface tension $\sigma_A = 1.5$ dyn/cm (top row) and $\sigma_A = 2.5$ dyn/cm (bottom row). For the low surface tension case, at high $c_s$ ($\approx 15$ mM), the electrostatic interactions are unable to overcome the elastic and surface tension forces making the nanocontainer retain its initial spherical conformation. As $c_s$ is lowered, the nanocontainer first deforms to a slightly ellipsoidal shape, and then to a prolate structure (rod) at $\approx 5$ mM. Such prolate nanocontainers were predicted to have lower energy compared to spherical nanocontainers of the same volume based on exact calculations considering only electrostatic interactions in the no-salt limit with purely Coulombic forces[39,44] (see Fig. 5C). Extensive parameter space exploration enables the identification of these rod-shaped nanocontainers as low-energy equilibrium shapes for the full model that incorporates screened electrostatic, elastic, and surface tension based interactions.

On further lowering of $c_s$ to 1 mM, a disc shape is obtained as the equilibrium nanocontainer conformation. This transition from prolate (aspect ratio $\lambda > 1$) to oblate ($\lambda < 1$) shapes in charged nanocontainers is, to the best of our knowledge, first reported here. As demonstrated above, the salt concentration of the solution (i.e., the ionic strength) serves as a viable control parameter for modulating this shape transition.

Figure 2 (bottom row) demonstrates that similar shape transitions are observed for the higher surface tension $\sigma_A = 2.5$ dyn/cm. Increasing the surface tension inhibits large deformation in all cases ($c_s$ values), thus yielding more modestly deformed rods and discs. Both salt concentration and surfactant concentration provide chemical means of controlling deformation by manipulating additives in the bulk solution, producing highly deformed discs at the extreme values of the parameters, or more modestly deformed rod and disc morphologies at intermediate $c_s$ and $\sigma_A$. We note that further enhancement of electrostatic interactions (e.g., by decreasing $c_s$) leads to the formation of bowls, as noted in our previous study[39].

Figure 3 demonstrates that the same shape can be realized in nanocontainers of different sizes. Here rod-shaped nanocontainers are generated from an initial spherical conformation with radii of $R = 10,15,20$ nm. The same shape at different sizes is engineered by changing both the chemical control (in this case, salt concentration) and the material design parameters (surface charge and elasticity). Similar variation in sizes is observed for disc-shaped (oblate) nanocontainers. Given the wide range of tunable chemical and material design parameters, such shape transitions are expected to occur at even larger sizes, thus enabling the synthesis of nanocontainers with diverse shape-size combinations.

## 3.2 Shape Maps

Simulations help rapidly investigate a multidimensional parameter (design) space to determine equilibrium shapes over a wide range of chemical control conditions for a given material composition. The shape map in Figure 4A shows the rods and discs of various aspect ratios predicted as equilibrium shapes depending on the salt concentration $c_s$ and surface tension $\sigma_A$. The specific values and domain of these control parameters over which shape transitions are observed is a function of the particle size $R$ (volume), net effective charge $Q$, and nanocontainer elastic moduli $\kappa_b$ and $\kappa_s$. For example, the shape map in Figure 4A is for nanocontainers of $R = 10$ nm, $Q = 600e$, and $\kappa_s = \kappa_b = 40k_BT$. Sphere-rod-disc shape transitions for these nanocontainers are generally observed between $\sigma_A \in [0,3.5]$ dyn/cm and $c_s \in [0,35]$ mM. As is evident from the shape map, for higher $\sigma_A$ values, only sphere-rod transitions are observed as $c_s$ is lowered down to $\lesssim 1$ mM. At intermediate $\sigma_A$ values, the full spectrum of sphere-rod-disc transitions are seen with varying $c_s$. However, at very low $\sigma_A \approx 0$, sphere-disc transitions dominate as $c_s$ is decreased, making the prolate (rod) conformations elusive. Similar analysis yields an easier visualization of shape transitions at fixed $c_s$ with surface tension as the control. Shape maps thus enable rapid inferences (look-ups) of parameters associated with desired equilibrium conformations (e.g., rods, discs of varying aspect ratios).

In addition to exploring the chemical control of shape transitions, simulations enable the study of equilibrium shapes as a function of tuning the elastic material properties. Associated material design principles complement the environmental control strategies for engineering shape adaptation in nanocontainers. Figure 4B shows a shape map exhibiting the dependence of the aspect ratio of the equilibrium nanocontainer shape on the stretching and bending moduli for a given set of chemical control parameters. Nanocontainer surface charge and volume are held fixed to $Q = 1050e$ and $V = 4/3\pi 20^3$ nm$^3$ respectively. At fixed $\kappa_s$, examining the aspect ratios as a function of $\kappa_b$ reveals interesting features reminiscent of using chemical controls to manipulate for shape transitions. For high $\kappa_s \gtrsim 30k_BT$, the sweep over the explored regime of $\kappa_b \in (5,40)k_BT$ produces predominantly sphere-disc transitions; rod-shaped conformations are not observed. On the other hand, for $20 < \kappa_s < 30k_BT$, clear sphere-rod-disc shape transitions are seen, with prolate nanocontainers dominant in the $\kappa_b \approx \kappa_s$ region, indicating the importance of low $\gamma = \kappa_s/\kappa_b$ (FvK number) for producing rod-shaped nanocontainers. Thus, the shape map in Figure 4B demonstrates the elastic moduli to be viable material design controls for modulating the

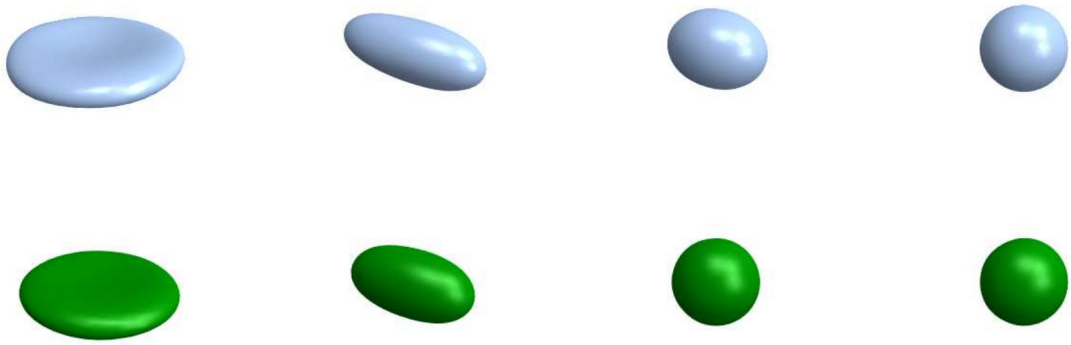

**Fig. 2** Simulation snapshots showing the change in equilibrium conformation of nanocontainers as the salt concentration $c_s$ is changed, with disc-rod-sphere transitions observed as $c_s$ increases left-to-right. The top row corresponds to a surface tension of $\sigma_A = 1.5$ dyn/cm, while bottom row is at a higher tension of $\sigma_A = 2.5$ dyn/cm. Increasing tension limits the extent of deformation of the nanocontainer. All nanocontainers have the same volume $V = 4/3\pi 10^3$ nm$^3$, effective charge $Q = 600e$, and elastic moduli $\kappa_b = \kappa_s = 40k_BT$. The salt concentration from left-to-right is $c_s = (1, 5, 10, 15)$ mM.

**Fig. 3** Rod formation persists for nanocontainers of different size, with nanocontainers from left-to-right having volumes of $V = 4/3\pi 10^3$ nm$^3$, $4/3\pi 15^3$ nm$^3$, and $4/3\pi 20^3$ nm$^3$, respectively (relative size shown to scale). The left-most rod shown has an effective charge $Q = 600e$, elastic moduli $\kappa_b = \kappa_s = 40k_BT$, and is in a solution with a salt concentration of $c_s = 5$ mM. The central rod shown has an effective charge $Q = 800e$, elastic moduli $\kappa_b = \kappa_s = 20k_BT$, and is in a solution with a salt concentration of $c_s = 1$ mM. The right-most rod shown has an effective charge $Q = 1050e$, elastic moduli $\kappa_b = \kappa_s = 20k_BT$, and is in a solution with a salt concentration of $c_s = 1$ mM. All nanocontainers have a surface tension of $\sigma_A = 2$ dyn/cm. Despite the decreasing charge density as the size increases, the deformation into rod-shaped structures persists.

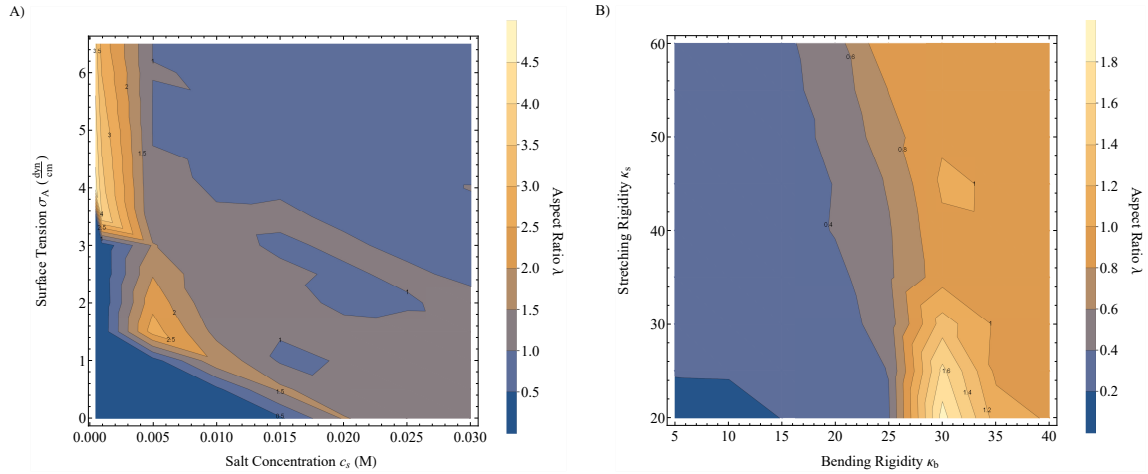


**Fig. 4** Shape maps displaying parameter regimes in which disc or rod morphologies are expected. A) A chemical control map displaying the shape that will result under a given concentration of salt and a given nanocontainer surface tension. This parameter dependence is expected of nanocontainers with constant volume $V = 4/3\pi 10^3$ nm$^3$, effective charge $Q = 600e$, and elastic parameters $\kappa_s = \kappa_b = 40 k_B T$. Aspect ratios $\lambda < 1$ indicate oblate discs, whereas $\lambda > 1$ indicate prolate rods. B) A material design control map demonstrating elasticity dependence, with higher bending rigidities preferring rod-like morphologies. The map corresponds to nanocontainers of volume $4/3\pi 20^3$ nm$^3$ and effective charge $Q = 1050e$ placed under solution conditions of salt concentration $c_S = 25$ mM and surface tension $\sigma_A = 0$ dyn/cm (resulting from high surfactant concentration).

preference for disc or rod morphologies.

We note that our earlier work[39] showed sphere-disc-bowl transitions for $\kappa_s = 100 k_B T$ and $\kappa_b \in (1, 10) k_B T$ (outside the exhibited range in the Figure 4B shape map). In the light of the more extensive exploration of the $\kappa_s, \kappa_b$ design space, we find that the bowl-shaped nanocontainers form for low $\kappa_b$ and high $\kappa_s$, that is, for high $\gamma \sim 10 - 100$ values. As we mentioned above, more moderate $\gamma \sim 5 - 10$ values yield relatively planar disc-like conformations. For low $\gamma \sim 1$, prolate-shaped nanocontainers are observed.

### 3.3 Shape control mechanisms: surface area and electrostatic energy

Under a constraint of fixed volume, shape transitions can only occur with an increase in nanocontainer area during deformation away from sphere (the latter has the least surface area for a given volume). All the shape transitions recorded in simulations exhibit an increase in the nanocontainer area. Figure 5A shows the ratio of the nanocontainer area relative to that of the sphere as a function of the salt concentration $c_s$ for a representative set of nanocontainers. Nanocontainers of two different sizes (volumes of $V = 4/3\pi 10^3$ nm$^3$ and $V = 4/3\pi 20^3$ nm$^3$), effective charges ($600e$ and $1050e$), and different material design parameters are selected. At high $c_s$, the equilibrium shape is closer to a sphere and the increase in area is small. As $c_s$ decreases, the area increases and approaches the highest values at the lowest $c_s$. In general, for the full sphere-rod-disc transition, rods have intermediate areas between spheres and discs.

Figure 5B shows the corresponding changes in the nanocontainer electrostatic energy as its area increases (Figure 5A). The total electrostatic energy of the final (equilibrium) nanocontainer relative to that of the initial sphere with identical parameters is plotted. The data is shown for the same representative set of material and chemical control parameters as in Fig. 5A. In all cases, this difference in electrostatic energy is negative, indicating that the decrease in electrostatic energy drives the shape deformation. Associated increase in area, as noted above, is penalized by a rise in stretching and bending energies. The resulting competition sets an effective area for the nanocontainer, and together with the volume constraint, sets the shape of the nanocontainer.

We previously performed exact analytical calculations on uniformly-charged as well as conducting (equipotential) spheroidal nanocontainers with unscreened Coulomb interactions ($1/r$ electrostatic forces). These calculations showed that the deformation of a sphere to both oblate (disc-like) or prolate (rod-like) structures under constraint of fixed volume are equally favorable[44]. Thus, the equilibrium solution in the case of these idealized systems is degenerate. This degeneracy is broken, and the system prefers disc-like (or rod-like) shapes when other interactions such as the elastic forces (bending, stretching) and surface tension compete with electrostatic forces to modulate the deformation. We discuss next the role of surface tension in the emergence of rod-shaped nanocontainers found in the above transitions under appropriate material and chemical control conditions.

The sum of unscreened Coulomb energy and surface tension energy, $U$, of idealized spheroidal nanocontainers under the constraint of fixed volume was evaluated exactly. For simplicity, conducting nanocontainers were considered, but the following arguments also hold for uniformly-charged systems. Further, in the wake of condensation of mobile counterions, under certain conditions, it is expected that the nanocontainer surface will be better approximated as a conducting surface.

For the case of disc-like nanocontainers (oblate spheroidal

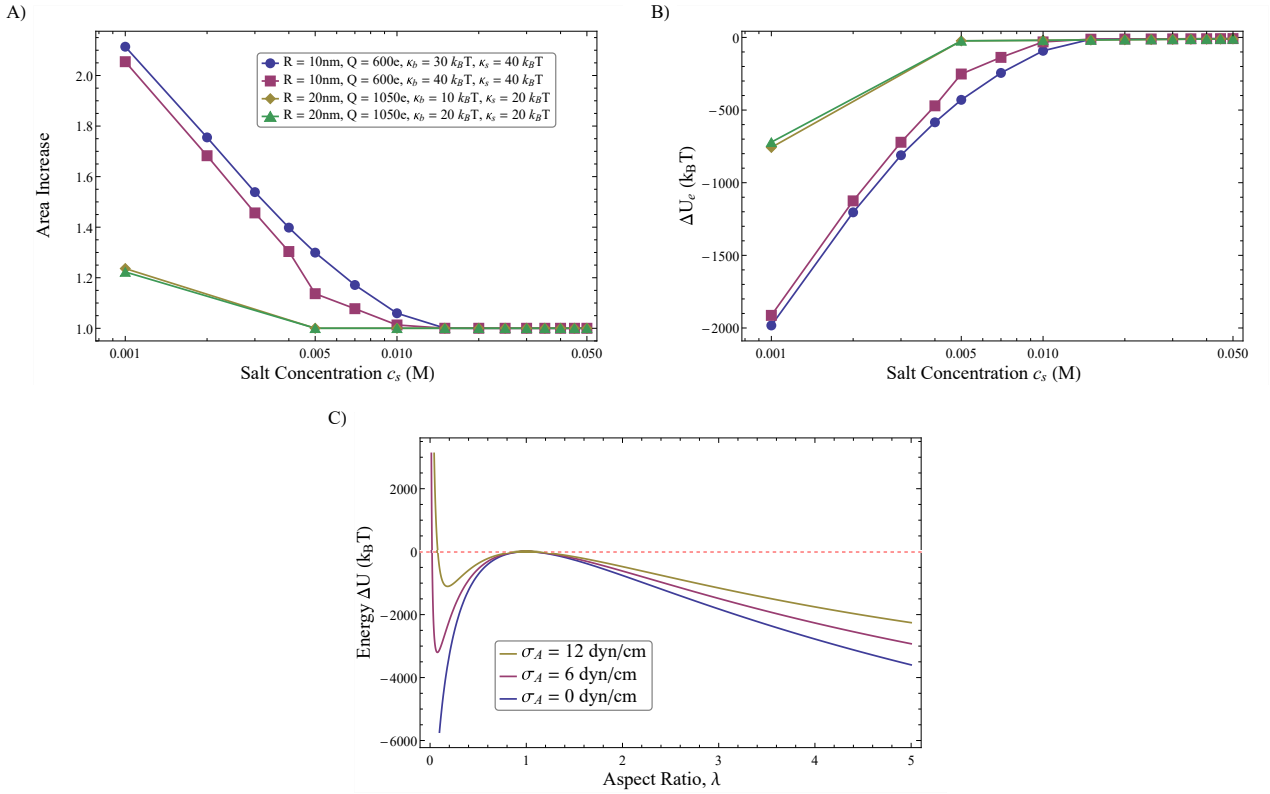


**Fig. 5** A) Nanocontainer area increases, under fixed volume constraint, as the sphere is deformed to spheroidal (e.g., rod, disc) structures for 4 different parameterizations (varying bending modulus) at two different volumes of nanocontainers. The ratio of the area of the nanocontainer to that of the sphere (of same volume) is plotted on the y-axis. Sufficient salt concentration inhibits deformation, whereas the area increase is significant at low salt concentration. The surface tension in each case is $\sigma_A = 1.5$ dyn/cm. B) The corresponding decrease in electrostatic energy driving the area change in (A). As area increases, the charge on the nanocontainer surface is further spread out, lowering the net electrostatic energy. C) Analytical calculation of the sum of electrostatic and tension energy (in the absence of salt, Eqs. 2 and 3) for a conducting spheroidal nanocontainer relative to the spherical nanocontainer ($\Delta U = U(\lambda) - U(1)$; see text) as a function of the aspect ratio $\lambda$ for different surface tension $\sigma_A$. As ($\lambda \to 0$) or ($\lambda \to \infty$), the energy ($\Delta U$) diverges to infinity due to the surface tension energy term. However, the approach is more gradual in the rod-shaped (prolate) conformations compared to the disc-shaped (oblate) structures such that rod becomes preferred under sufficient tension.

shells with aspect ratio $\lambda \leq 1$), $U = U_d$ is given by

$$U_d(\lambda) = \frac{l_B Q^2 \lambda^{1/3} \tan^{-1}\left(\frac{\sqrt{1-\lambda^2}}{\lambda}\right)}{2R\sqrt{1-\lambda^2}} + \sigma_A 2\pi R^2 \lambda^{-2/3}\left(1 + \frac{\lambda^2 \tanh^{-1}(\sqrt{1-\lambda^2})}{\sqrt{1-\lambda^2}}\right). \quad (2)$$

For rod-like nanocontainers (prolate spheroidal shells with aspect ratio $\lambda \geq 1$), $U = U_r$ is given by

$$U_r(\lambda) = \frac{l_B Q^2 \lambda^{1/3} \log\left(\lambda + \sqrt{\lambda^2-1}\right)}{2R\sqrt{\lambda^2-1}} + \sigma_A 2\pi R^2 \lambda^{-2/3}\left(1 + \frac{\lambda^2 \csc^{-1}\left(\frac{\lambda}{\sqrt{\lambda^2-1}}\right)}{\sqrt{\lambda^2-1}}\right). \quad (3)$$

Figure 5C shows the plot of the above energies relative to that of the sphere, i.e., it shows the energy difference $\Delta U = U(\lambda) - U(1)$ for $\lambda$ values spanning both disc-like and rod-like shapes. Conducting nanocontainers with charge $Q = 600e$ and radius $R = 10$ nm are considered; the electrostatic energy for the spherical conformation is $U_s^e \approx 18000 k_B T$. To illustrate the mechanisms behind the observed transition into rod-shaped structures, three representative cases characterized by surface tension $\sigma_A$ are considered: no surface tension ($\sigma_A = 0$), moderate surface tension ($\sigma_A = 6$ dynes/cm), and high surface tension ($\sigma_A = 12$ dynes/cm). It is assumed that there are no elastic energy penalties and the container is completely flexible.

In the absence of surface tension, as $\lambda \to 0$ (very flat disc) or $\lambda \to \infty$ (very thin rod), $\Delta U$ (which is determined solely by electrostatic energy for $\sigma_A = 0$) approaches a finite value of $-U_s^e$. In the presence of surface tension, e.g., for $\sigma_A = 6$ dynes/cm, as $\lambda \to 0$ or $\lambda \to \infty$, $\Delta U$ diverges to infinity. The divergence arises because the surface tension energy term approaches infinity (area diverges) in these extreme limits to conserve the nanocontainer volume. However, as the figure shows, the approach to infinity is more gradual for the rod-shaped nanocontainers compared to the disc-like ones. Thus rods may be preferred as the shape is deformed away from sphere, and indeed this is observed in Fig. 2.

The highest surface tension curve in Figure 5C exhibits this breaking of disc/rod degeneracy more clearly. A more shallow local energy minimum for disc-like conformations appears, indicating that electrostatics-driven shape change quickly becomes expensive if discs are the deformed structures. On the other hand, the energy continues to drop if the container adopts a rod-like shape. Overall, these results support the observation of shape transitions with more complex interactions (e.g. elastic, screened Coulomb potentials) by showing that inhibiting dramatic increase in nanocontainer area by enhancing surface tension biases the transitions in favor of rod-shaped nanocontainers.

### 3.4 Elastic energy distributions on the nanocontainer surface

Electrostatic interactions drive the transformation in the nanocontainer shape away from spherical conformation and towards shapes of aspect ratio $\lambda \neq 1$. Elastic energy (bending and stretching) and surface tension energy compete with electrostatic energy to generate oblate-shaped (disc-like; $\lambda < 1$) or prolate-shaped (rod-like; $\lambda > 1$) nanocontainers of varying eccentricities. We now examine changes in the distribution of the elastic energies on the nanocontainer surface after the nanocontainer adopts disc-like and rod-like conformations.

Figure 6 shows the local distribution of bending and stretching energies associated with typical disc-shaped and rod-shaped nanocontainers. For the disc, the outer "rim" or edge exhibits high bending energy while the central region shows almost zero bending energy (obvious by inspection that this part is "flat"). For the rod, the two terminating ends exhibit the highest bending energy. The central region of the rod shows greater bending energy compared to the central region of the disc.

The rod exhibits higher stretching energy along most of the surface away from the terminating ends; this is to be expected as the uniaxial stretching imparts the characteristic rod-like shape. On the disc-shaped nanocontainer, the stretching energy is effectively uniform with striations arising from the pentameric defects in the icosahedrally symmetric mesh. Thus the shape transition in nanocontainers to prolate or oblate structures is accompanied by non-uniform distributions of bending and stretching elastic energies on the nanocontainer surface.

### 3.5 Counterion Condensation

The shape transitions recorded via the MD-based simulated annealing procedure were obtained using a Yukawa potential to model the electrostatic interactions characterizing the nanocontainer surface, with the effects of salt ions treated implicitly. The condensation of counterions on the nanocontainer surface can alter these shape transitions. We now examine the effects of counterion condensation on the feasibility of the observed transitions.

Deviations from linearized Poisson-Boltzmann (Debye-Huckel) theory are expected for highly-charged nanocontainers where the Gouy-Chapman length $b \ll \lambda_D$. For the salt concentrations examined in the simulations, we get $1 < \lambda_D < 10$ nm; and for the charge densities probed in this work $0.1e/\text{nm}^2 < \sigma_b < 0.5e/\text{nm}^2$, we obtain $0.5 < b < 2$ nm. Thus, deviations from the linearized electrostatic model are expected to be strong for the nanocontainer with the highest charge density (of $\sigma_b = 0.48e/\text{nm}^2$ with $Q = 600e$ and $R = 10$ nm). These deviations can be ascribed to charge renormalization caused by the condensation of counterions and associated effects have been investigated by Manning and others for uniformly-charged (as well as equipotential) nanoparticle surfaces modeled as spheres, cylinders, and planes[67,68]. Recent research based on nonlinear Poisson-Boltzmann effects and explicit ion Monte Carlo simulations suggest that in highly-charged nanomembranes, under very weak screening limit ($\lambda_D > R$), counterion release can provide a force to stabilize spherical conformations and alter the nature of these shape transitions[63]. In

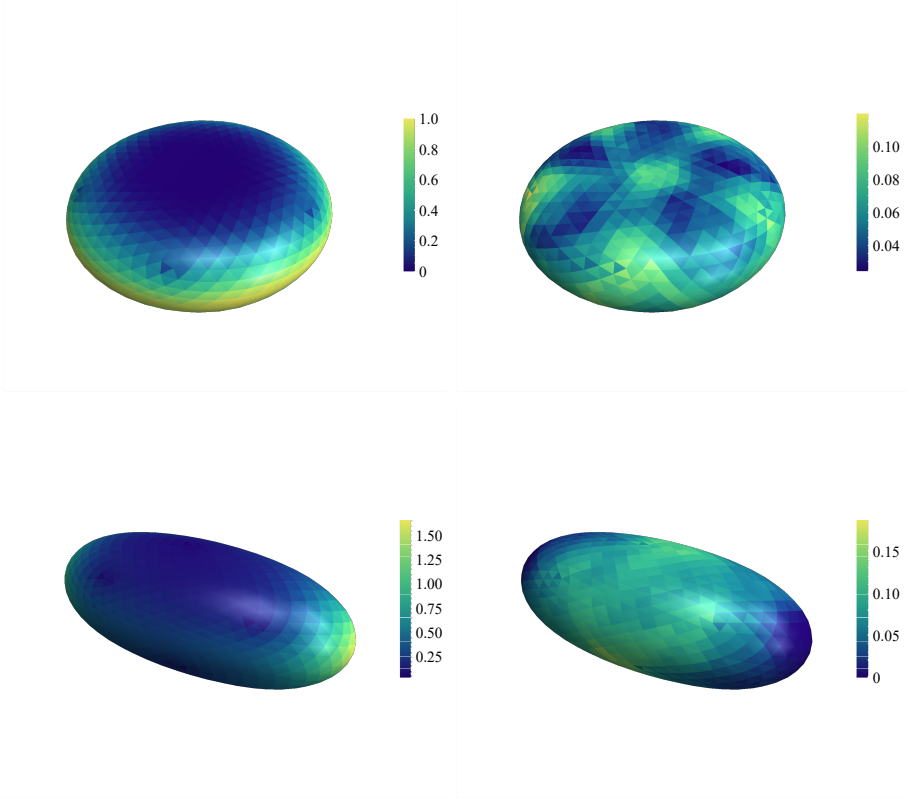


**Fig. 6** Distribution of bending (left column) and stretching elastic energies (right column) on the surface of the nanocontainer upon deformation to a typical disc-like/oblate shape (top row) and a typical rod-like/prolate shape (bottom row). Each nanocontainer shown has a volume $V = 4/3\pi 10^3$ nm$^3$, charge $Q = 600e$, stretching rigidity $\kappa_s = 40k_BT$, and it is placed in a solution with a salt concentration of $c_s = 5$ mM. All scale bars are in units of $k_BT$. (Top Left) Bending energy distribution on the surface of the disc-shaped nanocontainer with aspect ratio $\lambda \approx 0.3$ and bending rigidity $\kappa_b = 30k_BT$. (Top Right) Stretching energy distribution on the same disc is effectively uniform with striations dominated by the pentameric defects in the mesh. (Bottom Left) Bending energy distribution on the surface of the rod-shaped nanocontainer with aspect ratio $\lambda \approx 2.74$ and increased bending modulus $\kappa_b = 40k_BT$. (Bottom Right) Stretching energy distribution on the same rod showing that the majority of the rod away from the ends has higher stretching energy as the latter redistributes to support bending at the terminal ends.

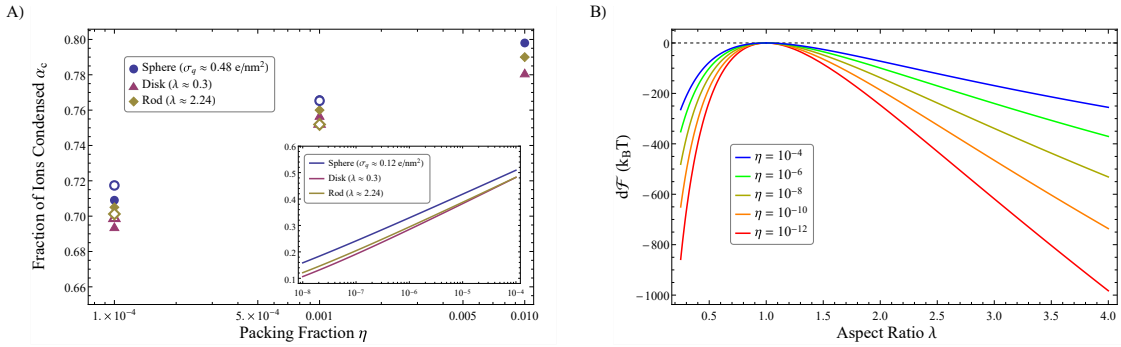


**Fig. 7** Assessment of the effects of ion condensation on nanocontainer shape deformation. A) Fraction of condensed ions $\alpha_c$ from explicit ion simulations (closed symbols) are in close agreement with the Manning two-state model (open symbols) in the no-salt limit for shapes of volume $V = 4/3\pi(10)^3$ nm$^3$ and surface charge density $\sigma_b = 0.48e/\text{nm}^2$, even at relatively high packing fractions up to ($\eta = 10^{-3}$). The disc and rod used were of aspect ratio $\lambda \approx 0.3, 2.24$, respectively. Inset) $\alpha_c$ from Manning model for the nanocontainer with $\sigma_b = 0.12e/\text{nm}^2$, $V = 4/3\pi(20)^3$ nm$^3$, and proportionally larger disc and rod of the same aspect ratio as before. This plot shows that condensation effects are weaker for lower $\sigma_b$ and lower $\eta$. B) Manning model estimates of the free energy change as a function of aspect ratio, $d\mathcal{F}(\lambda)$, between the spherical nanocontainer with $R = 10$ nm, $Q = 600e$, $\sigma_b = 0.48e/\text{nm}^2$ ($\lambda = 1$) and the deformed structure ($\lambda \neq 1$), under variable packing fractions $\eta$. This demonstrates that while deformation is certainly favored at low packing fractions (by several hundred $k_BT$), it remains favorable even at higher packing fractions.

our studies, this limit is reached for the aforementioned nanocontainer with $\sigma_b = 0.48e/\text{nm}^2$ at low salt concentrations ($c_s \sim 1$ mM).

The effects of counterion condensation are enhanced at higher nanocontainer bare charge density $\sigma_b$, lower salt concentration $c_s$, and higher packing fraction $\eta$ (nanocontainer concentration). We first examine the effects of ion condensation on shapes of nanocontainers with high charge density (Fig. 1, $\sigma_b \approx 0.48$ $e/\text{nm}^2$, $Q = 600e$, $R = 10$ nm) with no added salt (thus considering a worse-case scenario). Following the procedures outlined in Section 2, equilibrium MD simulations of counterions near these nanocontainers of different shapes were performed using LAMMPS for a variety of packing fractions. The fraction of condensed counterions was extracted following the equation: $\alpha_c = N_c/N_{tot}$, where $N_{tot}$ is the total number of ions and $N_c$ is the number of condensed ions. Using $\alpha_c$, the effective charge for the nanocontainer can be defined as $Q = Q_{bare} - z_i N_c$, where $z_i$ is the valence of the counterion and $Q_{bare}$ is the bare charge of the nanocontainer. Note, electroneutrality dictates that $N_{tot} = Q_{bare}/z_i$ in the absence of salt.

Figure 7A shows the estimates of the fraction of condensed counterions, $\alpha_c$, from these explicit ion simulations near a disc ($\lambda \approx 0.3$), rod ($\lambda \approx 2.24$), and sphere ($\lambda = 1$) of equal volume (associated with the sphere of radius $R = 10$ nm). The disc and the rod considered in this study are significantly deformed. Estimates are shown for three $\eta$ values ($10^{-4}, 10^{-3}, 10^{-2}$); simulations at lower $\eta$ (more dilute) were prohibitively expensive due to the slow dynamics of ions towards equilibration. At all packing fractions studied, more counterions condensed on the sphere than the rod and the disc, the latter exhibiting the lowest counterion condensation in agreement with recent results[63]. However, the deformed shapes with higher (or lower) aspect ratios exhibited $\alpha_c$ values $\mathcal{O}(1)$ percent less than those for the spherical structure. The effective charge as well as the number of released counterions across the different shapes (disc, rod, sphere) were very similar, implying that the difference between shapes do not produce significantly different condensation effects and hence these effects are expected to not alter the nature of observed shape transitions.

In addition to explicit ion simulations, following our earlier work[39,44], we performed mean-field calculations based on the Manning two-state model[67] to obtain analytical estimates for $\alpha_c$. Idealized spheroidal-shaped nanocontainers (both rods and discs) with conducting surfaces (similar to the systems employed in Sec. 3.3 for exact analytical solutions) were used in the calculations. Following the Manning model approximation, we write the free energy of the nanocontainer-ion system as

$$\begin{aligned}\mathscr{F}(\alpha_c,\lambda) = U(\lambda,\alpha_c) + \alpha_c N_{tot} log\left(\frac{\alpha_c N_{tot}\Lambda^3}{A(\lambda,R)b}\right) - \alpha_c N_{tot} \\ +(1-\alpha_c)N_{tot} log\left(\frac{(1-\alpha_c)N_{tot}\Lambda^3}{V_{WS}}\right) - (1-\alpha_c)N_{tot},\end{aligned} \tag{4}$$

where $U(\lambda,\alpha_c)$ is the electrostatic potential energy of the spheroidal nanocontainer given by Equations 2 or 3; electrostatic energy terms dominate the total potential energy $U$. The next two terms represent entropic contributions of the $\alpha_c N_{tot}$ condensed ions to the free energy, and the last two terms correspond to the entropy of the $(1-\alpha_c)N_{tot}$ free (released) ions in the bulk solution. $N_{tot}$ is the number of counterions, $\Lambda$ is the thermal de Broglie wavelength, $A(\lambda,R)$ is the surface area of the spheroid, $b = 1/(2\pi l_B \sigma_b)$ is the Guoy-Chapman length set by the bare surface charge density $\sigma_b$, and $V_{WS}$ is the volume of the electroneutral Wigner-Seitz cell set by the packing fraction of the nanoparticles. The fraction of ions condensed is computed as the value that minimizes the above free energy. The condensation behavior and resulting free energy are a function of the shape (size $R$, aspect ratio $\lambda$) and the bare charge $Q_{bare}$.

Results for $\alpha_c$ using the Manning two-state model were in good agreement with explicit ion simulation results for $\eta = 10^{-4}, 10^{-3}$ as shown in the Fig. 7A. Manning model is expected to provide more accurate estimates for $\alpha_c$ and associated free energy of the charge-renormalized nanocontainer at lower packing fractions. Utilizing this scenario, $\alpha_c$ and the free energy $dF$ of nanocontainer (relative to the spherical conformation) were computed; the latter is plotted in Figure 7B. As the figure shows, for $\eta \in (10^{-12}, 10^{-4})$, the free energy of the spheroidal structure is lower compared to the spherical shape ($dF < 0$), indicating that the shape transitions are feasible in the wake of ion condensation for a broad range of packing fractions up to $\eta = 10^{-4}$.

The high value of $\alpha_c$ shown in Figure 7A implies that the effective charge is significantly reduced compared to the bare charge. The shape transitions shown in Fig. 2 assume an effective charge of $Q = 600e$. We next examine nanocontainers with a lower surface charge density $\sigma_b = 0.12e/\text{nm}^2$ (same charge $Q = 600e$ and a larger volume $V = 4/3\pi 20^3$ nm$^3$), and use the Manning model to predict the fraction of condensed ions. Sphere, disc, and rod of similar aspect ratios as in the previous study are considered; these are produced using the shape optimization procedure for a different set of material and chemical control parameters. The inset of Figure 7A shows the change in $\alpha_c$ as a function of the packing fraction in the range $(10^{-8}, 10^{-4})$. Dilute systems ($\eta \lesssim 10^{-7}$) show a very low fraction of condensed ions, demonstrating that the effects of ion condensation are diminished for nanocontainers with lower $\sigma_b$ at lower packing fractions. The difference in $\alpha_c$ across different shapes for the systems considered in the inset of Fig. 7A remains on the order of a few percent.

We note that the study of condensation effects based on the above two-state Manning model employs a number of approximations. For example, the free energy associated with this model does not take into account the counterion-nanocontainer and counterion-counterion Coulomb interactions explicitly. Also, the distribution of counterions around the spheroidal shell is considered to be isotropic, which is an oversimplification for shapes that deviate significantly from the spherical conformation. In this light, we view the above Manning model results as qualitative. Quantitative results that address many of the aforementioned simplifications can be obtained by adopting a unified approach to combine the shape optimization dynamics and the ion dynamics in a single MD procedure. Developing this unified approach is part of our future work.

## 4 Conclusion and Future Work

The above results reveal the fundamental mechanisms of engineering adaptive shape control in charged deformable nanocontainers by modulating their surface properties (e.g., charge, tension, elastic constants), and environmental conditions. The wide coverage of the multidimensional parameter space yields a rich gallery of shapes, including rods and discs of various aspect ratios, that can be tailored by judiciously selecting material features and environmental conditions. These shape maps guide the design of deformable nanocontainers that actively change shape in response to evolving environmental conditions. They can also be useful in experimental and computational materials chemistry studies aimed at engineering functional nanoparticles by controlling their intrinsic design features.

Both environmental solution conditions and materials design control strategies are demonstrated as viable means to generate shape change in nanocontainers. Bulk solution control strategies can include tuning salt concentration that affects the screening length associated with the electrostatic interactions, and tuning surfactant concentration that changes the interfacial surface tension (hydrophobicity). Material design strategies may consist of modulating the particle size, charge, and elasticity. Each of these control strategies is capable of modulating the favorability of deformation into oblate discs, prolate rods, or spherical morphologies.

Environmental conditions such as salt and surfactant concentration determine the extent of deformation and, at times, the qualitative distinction between disc and rod formation. For example, increasing salt concentration can change significantly-deformed discs into modestly-deformed rods of lower surface area (Figs. 2 and 4A). Modulating material properties also affects the bias towards disc/rod morphologies; discs and rods occur depending on the ratio of the bending and stretching moduli, (Fig. 4B). The emergence of rod-like shapes under appropriate surface tension was also shown using exact analytical results on conducting nanocontainers under no-salt conditions (Fig. 5C).

To assess the stability of the observed shape transitions of charged nanocontainers in the event of counterion condensation, we extended our previous work[39,44] that used mean-field Manning model calculations to examine ion condensation effects. This extension makes use of simulations of explicit counterions near nanocontainers under no-salt conditions to evaluate the fraction of condensed ions. This fraction and the resulting nanocontainer effective charge $Q$ changes by a small amount, $\approx 1\%$, between spherical and disc/rod conformations up to the nanocontainer packing fraction of $10^{-2}$ for the highest charge density studied (Fig. 7A). Good agreement of the MD results with Manning model results enabled the computation of approximate free energy differences between the spherical and spheroidal shapes for moderate values of packing fractions ($10^{-12} - 10^{-4}$). This analysis showed the disc and rod-shaped structures are also favored in the event of condensation (Fig. 7B). Ion condensation effects are shown to be weaker for lower nanocontainer packing fractions and lower surface charge density, and these effects are expected to weaken further with increasing salt concentration. Condensation effects are expected to also be mitigated by judiciously adapting the material features such as the elastic moduli.

More accurate predictions for feasible and stables shapes can be made by adopting a unified approach of minimizing the energy characterizing the nanocontainer in the presence of explicit counterions. Designing this combined approach will be a subject of future studies and we expect it to yield more accurate estimates for the fraction of condensed ions while more precisely evaluating the electrostatics-driven shape deformation. Future work will also consist of expanding upon chemical and materials design control strategies by investigating the potential of surface charge patterning to alter the shape deformation[69]. This will involve investigating designed charge patterns (e.g., alternating positive and negative Janus-like nanocontainers) as well as pH-driven stochastic charge patterns for generating shapes. Further, future plans involve extending the studies to investigate real-time shape evolution, enabling estimates of the time scale of nanocontainer shape switching in response to environmental conditions or thermal activation. Time scales for deformation are an experimentally measurable and relevant quantity[29,70].

We now highlight experimental studies that may involve the electrostatics-driven shape transitions and control mechanisms revealed in this work, and also point out the limitations in the scope of our investigations. Recent experiments on the self-assembly of viruses such as hepatitis B virus, which exhibits a relatively small bending rigidity[71], have shown that virus subunits in the presence of drug molecules assemble into nanocontainers (hollow protein cages of radius $\approx 18-40$ nm) that exhibit a transition from normal (spheres) to aberrant shapes (ellipsoidal, cylindrical) as the ionic strength is decreased[72]. The shape transitions as a function of ionic strength suggest electrostatic control mechanisms changing the association energy driving the protein self-assembly. However, we note that the volume of the observed nanostructures is not conserved in these experiments.

Experiments with solid block copolymer nanoparticles assembled using mixed functional surfactants into morphologies that range from sphere to prolate ellipsoids show that the ellipsoidal particles respond to changes in pH over a broad range from 3 to 10. Tuning the pH alters the charge on the polymer chains that results in prolate ellipsoidal structures of different aspect ratios; these pH-triggered shape changes are also shown to be reversible[73]. We anticipate our computational studies to inform future experiments on exploring electrostatically-controlled shape transitions in similar soft-matter systems such as virus nanoparticles, micellar nanomembranes, and polymeric vesicles.

We also note that there are several experimental studies that demonstrate nanoparticle shape change driven by different mechanisms (that often dominate over electrostatic forces) such as entropic forces and surface tension[29,31]. For example, the shape transformation of PEGylated polymer/DNA nanoparticles from worm-like to short-rods to spheres upon PEG cleavage is primarily driven by the competition between the maximization of PEG entropy and DNA-solvent interfacial tension[31]. Despite strong DNA-polymer electrostatic forces as well as high surface charges observed for spherical morphologies, the electrostatic interactions only weakly affect the shape-switching process[74].

Self-assembly of nanoparticle building blocks into hierarchical clusters is of broad interest to the materials science community, and the close packing of rigid spherical and non-spherical building blocks has been extensively explored [17,75]. The links between surface features and equilibrium shapes can be leveraged in experiments and simulations on the self-assembly of deformable (flexible) nanoscale building blocks. Shape-changing properties of building blocks can enable the design of novel hierarchical structures with potential applications in medicine and catalysis. Further, the molecular dynamics simulation methods employed in this work can be extended to understand shape deformations and associated self-assembly mechanisms of microscale colloidal particles [26].

## Conflicts of interest

There are no conflicts to declare.

## Acknowledgements

This material is based upon work supported by the National Science Foundation under Grant No. DMR-1753182. Simulations were performed using the Big Red II supercomputing system supported in part by Lilly Endowment, Inc., through its support for the IU Pervasive Technology Institute, and in part by the Indiana METACyt Initiative.

## References

1 N. S. Abadeer and C. J. Murphy, *The Journal of Physical Chemistry C*, 2016, **120**, 4691–4716.

2 Y. Liu, J. Tan, A. Thomas, D. Ou-Yang and V. R. Muzykantov, *Therapeutic Delivery*, 2012, **3**, 181–194.

3 B. D. Chithrani, A. A. Ghazani and W. C. Chan, *Nano Letters*, 2006, **6**, 662–668.

4 D. B. Chithrani, *Molecular Membrane Biology*, 2010, **27**, 299–311.

5 J. Deng and C. Gao, *Nanotechnology*, 2016, **27**, 412002.

6 S. E. Gratton, P. A. Ropp, P. D. Pohlhaus, J. C. Luft, V. J. Madden, M. E. Napier and J. M. DeSimone, *Proceedings of the National Academy of Sciences*, 2008, **105**, 11613–11618.

7 P. Kolhar and S. Mitragotri, *Advanced Functional Materials*, 2012, **22**, 3759–3764.

8 Z. P. Xu, M. Niebert, K. Porazik, T. L. Walker, H. M. Cooper, A. P. Middelberg, P. P. Gray, P. F. Bartlett and G. Q. M. Lu, *Journal of Controlled Release*, 2008, **130**, 86–94.

9 A. K. Gupta and M. Gupta, *Biomaterials*, 2005, **26**, 1565–1573.

10 S. Mitragotri and J. Lahann, *Nature Materials*, 2009, **8**, 15.

11 Y. Geng, P. Dalhaimer, S. Cai, R. Tsai, M. Tewari, T. Minko and D. E. Discher, *Nat Nano*, 2007, **2**, 249–255.

12 S. Muro, C. Garnacho, J. A. Champion, J. Leferovich, C. Gajewski, E. H. Schuchman, S. Mitragotri and V. R. Muzykantov, *Molecular Therapy*, 2008, **16**, 1450–1458.

13 Y. He and K. Park, *Molecular Pharmaceutics*, 2016, **13**, 2164–2171.

14 S. Muro, C. Garnacho, J. A. Champion, J. Leferovich, C. Gajewski, E. H. Schuchman, S. Mitragotri and V. R. Muzykantov, *Molecular Therapy*, 2008, **16**, 1450–1458.

15 P. L. Chariou, K. L. Lee, J. K. Pokorski, G. M. Saidel and N. F. Steinmetz, *The Journal of Physical Chemistry B*, 2016, **120**, 6120–6129.

16 M. Youssef, T. Hueckel, G.-R. Yi and S. Sacanna, *Nature Communications*, 2016, **7**, 12216.

17 R. L. Marson, T. D. Nguyen and S. C. Glotzer, *MRS Communications*, 2015, **5**, 397–406.

18 T. D. Nguyen and S. C. Glotzer, *ACS Nano*, 2010, **4**, 2585–2594.

19 M. Uchida, K. McCoy, M. Fukuto, L. Yang, H. Yoshimura, H. M. Miettinen, B. LaFrance, D. P. Patterson, B. Schwarz, J. A. Karty, P. E. Prevelige, B. Lee and T. Douglas, *ACS Nano*, 2018, **12**, 942–953.

20 N. E. Brunk, M. Uchida, B. Lee, M. Fukuto, L. Yang, T. Douglas and V. Jadhao, *ACS Applied Bio Materials*, 2019, **2**, 2192–2201.

21 R. K. Cersonsky, G. van Anders, P. M. Dodd and S. C. Glotzer, *Proceedings of the National Academy of Sciences*, 2018, **115**, 1439–1444.

22 J. Sun, C. DuFort, M.-C. Daniel, A. Murali, C. Chen, K. Gopinath, B. Stein, M. De, V. M. Rotello, A. Holzenburg, C. C. Kao and B. Dragnea, *Proceedings of the National Academy of Sciences*, 2007, **104**, 1354–1359.

23 V. N. Manoharan, *Science*, 2015, **349**, 1253751.

24 E. Prodan, C. Radloff, N. J. Halas and P. Nordlander, *Science*, 2003, **302**, 419–422.

25 S. Sacanna, M. Korpics, K. Rodriguez, L. Colón-Meléndez, S.-H. Kim, D. J. Pine and G.-R. Yi, *Nature Communications*, 2013, **4**, 1688.

26 S. Sacanna, D. J. Pine and G.-R. Yi, *Soft matter*, 2013, **9**, 8096–8106.

27 F. Gröhn, *Soft Matter*, 2010, **6**, 4296–4302.

28 M. Youssef, T. Hueckel, G.-R. Yi and S. Sacanna, *Nature Communications*, 2016, **7**, 12216.

29 J.-W. Yoo and S. Mitragotri, *Proceedings of the National Academy of Sciences*, 2010, **107**, 11205–11210.

30 K. Zhou, Y. Wang, X. Huang, K. Luby-Phelps, B. D. Sumer and J. Gao, *Angewandte Chemie International Edition*, 2011, **50**, 6109–6114.

31 J.-M. Williford, Y. Ren, K. Huang, D. Pan and H.-Q. Mao, *Journal of Materials Chemistry B*, 2014, **2**, 8106–8109.

32 H. S. Seung and D. R. Nelson, *Phys. Rev. A*, 1988, **38**, 1005–1018.

33 J. Lidmar, L. Mirny and D. R. Nelson, *Phys. Rev. E*, 2003, **68**, 051910.

34 E. H. Yong, D. R. Nelson and L. Mahadevan, *Phys. Rev. Lett.*, 2013, **111**, 177801.

35 R. Sknepnek, G. Vernizzi and M. Olvera de la Cruz, *Soft Matter*, 2012, **8**, 636–644.

36 S. S. Datta, S.-H. Kim, J. Paulose, A. Abbaspourrad, D. R. Nelson and D. A. Weitz, *Phys. Rev. Lett.*, 2012, **109**, 134302.

37 F. Grohn, *Soft Matter*, 2010, **6**, 4296–4302.

38 R. Sknepnek, G. Vernizzi and M. O. de la Cruz, *Phys. Rev. Lett.*, 2011, **106**, 215504.

39 V. Jadhao, C. K. Thomas and M. O. de la Cruz, *Proceedings of the National Academy of Sciences*, 2014, **111**, 12673–12678.

40 M. Winterhalter and W. Helfrich, *The Journal of Physical Chemistry*, 1988, **92**, 6865–6867.

41 A. Lau and P. Pincus, *Physical Review Letters*, 1998, **81**, 1338.

42 D. Andelman, *Handbook of Biological Physics*, 1995, **1**, 603–642.

43 G. Vernizzi and M. Olvera de la Cruz, *Proceedings of the National Academy of Sciences*, 2007, **104**, 18382–18386.

44 V. Jadhao, Z. Yao, C. K. Thomas and M. O. De La Cruz, *Physical Review E*, 2015, **91**, 032305.

45 N. E. Brunk, J. Kadupitiya, M. Uchida, T. Douglas and V. Jadhao, *Nanoparticle Assembly Lab*, 2019, `https://nanohub.org/resources/npassemblylab`.

46 H. Seung and D. R. Nelson, *Physical Review A*, 1988, **38**, 1005.

47 Y. Kantor, M. Kardar and D. R. Nelson, *Physical Review Letters*, 1986, **57**, 791.

48 G. A. Vliegenthart and G. Gompper, *Biophysical Journal*, 2006, **91**, 834–841.

49 A. Šarić and A. Cacciuto, *Physical Review Letters*, 2012, **108**, 118101.

50 M. A. Greenfield, L. C. Palmer, G. Vernizzi, M. O. d. l. Cruz and S. I. Stupp, *Journal of the American Chemical Society*, 2009, **131**, 12030–12031.

51 R. Sknepnek, G. Vernizzi and M. O. de la Cruz, *Soft Matter*, 2012, **8**, 636–644.

52 R. Capovilla, J. Guven and E. Rojas, *Journal of Physics A: Mathematical and General*, 2005, **38**, 8841.

53 E. Beltrán-Heredia, V. G. Almendro-Vedia, F. Monroy and F. J. Cao, *Frontiers in physiology*, 2017, **8**, 312.

54 G. Gueguen, N. Destainville and M. Manghi, *Soft matter*, 2017, **13**, 6100–6117.

55 J.-P. Ryckaert, G. Ciccotti and H. J. Berendsen, *Journal of Computational Physics*, 1977, **23**, 327 – 341.

56 D. Z. Keifer, E. E. Pierson, J. A. Hogan, G. J. Bedwell, P. E. Prevelige and M. F. Jarrold, *Rapid Communications in Mass Spectrometry*, 2014, **28**, 483–488.

57 D. Z. Keifer, T. Motwani, C. M. Teschke and M. F. Jarrold, *Journal of the American Society for Mass Spectrometry*, 2016, **27**, 1028–1036.

58 W. K. Kegel and P. van der Schoot, *Biophysical Journal*, 2004, **86**, 3905–3913.

59 W. Roos, R. Bruinsma and G. Wuite, *Nature Physics*, 2010, **6**, 733.

60 J. Snijder, K. Radtke, F. Anderson, L. Scholtes, E. Corradini, J. Baines, A. J. Heck, G. J. Wuite, B. Sodeik and W. H. Roos, *Journal of Virology*, 2017, **91**, e00123–17.

61 M. G. van Rosmalen, C. Li, A. Zlotnick, G. J. Wuite and W. H. Roos, *Biophysical Journal*, 2018, **115**, 1656–1665.

62 W. R. Inc., *Mathematica, Version 12.0*, Champaign, IL, 2019.

63 Y. Jho, J. Landy and P. Pincus, *ACS Macro Letters*, 2015, **4**, 640–644.

64 R. W. Hockney and J. W. Eastwood, *Computer simulation using particles*, crc Press, 1988.

65 S. Plimpton, *Journal of Computational Physics*, 1995, **117**, 1 – 19.

66 A. Diehl and Y. Levin, *The Journal of Chemical Physics*, 2004, **121**, 12100–12103.

67 G. S. Manning, *The Journal of Physical Chemistry B*, 2007, **111**, 8554–8559.

68 S. Alexander, P. Chaikin, P. Grant, G. Morales, P. Pincus and D. Hone, *The Journal of Chemical Physics*, 1984, **80**, 5776–5781.

69 R. M. Adar, D. Andelman and H. Diamant, *Advances in Colloid and Interface Science*, 2017, **247**, 198–207.

70 T. Gong, K. Zhao, W. Wang, H. Chen, L. Wang and S. Zhou, *Journal of Materials Chemistry B*, 2014, **2**, 6855–6866.

71 P. Moerman, P. Van Der Schoot and W. Kegel, *The Journal of Physical Chemistry B*, 2016, **120**, 6003–6009.

72 P. Kondylis, C. J. Schlicksup, N. E. Brunk, J. Zhou, A. Zlotnick and S. C. Jacobson, *Journal of the American Chemical Society*, 2018, **141**, 1251–1260.

73 D. Klinger, C. X. Wang, L. A. Connal, D. J. Audus, S. G. Jang, S. Kraemer, K. L. Killops, G. H. Fredrickson, E. J. Kramer and C. J. Hawker, *Angewandte Chemie International Edition*, 2014, **53**, 7018–7022.

74 X. Jiang, W. Qu, D. Pan, Y. Ren, J.-M. Williford, H. Cui, E. Luijten and H.-Q. Mao, *Advanced Materials*, 2013, **25**, 227–232.

75 S. C. Glotzer, M. J. Solomon and N. A. Kotov, *AIChE Journal*, 2004, **50**, 2978–2985.